Mon. Not. R. Astron. Soc. **000**, 1–7 (2002) Printed 14 October 2015 (MN LATEX style file v2.2)

The mass of the very massive binary WR21a⋆

F. Tramper[1], H. Sana[2], N.E. Fitzsimons[1], A. de Koter[1,2], L. Kaper[1], L. Mahy[3], A. Moffat[4]

[1] *Anton Pannenkoek Institute for Astronomy, University of Amsterdam, 1090 GE Amsterdam, The Netherlands*
[2] *Instituut voor Sterrenkunde, Universiteit Leuven, Celestijnenlaan 200 D, B-3001, Leuven, Belgium*
[3] *Institut d'Astrophysique, Universite de Liège, Allée du 6 Août 17, B-4000 Liège, Belgium*
[4] *Départment de Physique, Université de Montréal and Centre de Recherche en Astrophysique du Québec, C. P. 6128, succ. centre-ville, Montréal (Qc)*

arXiv:1510.03609v1 [astro-ph.SR] 13 Oct 2015

—. —; —

ABSTRACT

We present multi-epoch spectroscopic observations of the massive binary system WR21a, which include the January 2011 periastron passage. Our spectra reveal multiple SB2 lines and facilitate an accurate determination of the orbit and the spectral types of the components. We obtain minimum masses of 64.4 ± 4.8 $M_\odot$ and 36.3 ± 1.7 $M_\odot$ for the two components of WR21a. Using disentangled spectra of the individual components, we derive spectral types of O3/WN5ha and O3Vz ((f*)) for the primary and secondary, respectively. Using the spectral type of the secondary as an indication for its mass, we estimate an orbital inclination of $i = 58.8 \pm 2.5°$ and absolute masses of 103.6 ± 10.2 $M_\odot$ and 58.3 ± 3.7 $M_\odot$, in agreement with the luminosity of the system. The spectral types of the WR21a components indicate that the stars are very young (1−2 Myr), similar to the age of the nearby Westerlund 2 cluster. We use evolutionary tracks to determine the mass-luminosity relation for the total system mass. We find that for a distance of 8 kpc and an age of 1.5 Myr, the derived absolute masses are in good agreement with those from evolutionary predictions.

Key words: binaries: close – binaries: spectroscopic – stars: early-type – stars: fundamental parameters – stars: individual (WR21a) – stars: Wolf-Rayet

1 INTRODUCTION

Massive stars are predominantly found in binary systems, with an intrinsic multiplicity fraction among the O-star population larger than 90% (e.g., Sana et al. 2014). The orbital properties of massive close binary systems provide a means to address one of the most intriguing open problems in massive star research: how massive can a star be? If there is an upper mass limit, its value may be dependent on environmental conditions and whether the star forms in solitude or as part of a multiple system. It could be envisioned that the upper mass limit for the components of binary systems is different than for single stars.

While an upper mass limit of 150 $M_\odot$ for presumed single stars has been derived by Figer (2005) based on a photometric analysis of the Arches cluster ($Z \approx 2Z_\odot$), stars well in excess of 150 $M_\odot$ have been identified in the core of the R136 region in the Large Magellanic Cloud ($Z \approx 0.5Z_\odot$; the most massive one being R136-a1, with an estimated current mass of 265 $M_\odot$; Crowther et al. 2010).

However, the masses of these stars cannot be estimated from their spectral characteristics, as their hydrostatic layers are obscured by their dense stellar winds (de Koter et al. 1997). Instead their masses are inferred from their luminosities, and are model dependent. The luminosities can also be affected by a contribution from unresolved stars if the field is crowded, or by uncertainties in extinction (e.g., Bestenlehner et al. 2011). The orbital motion of binaries in which one or both of the components is a very massive star allows for accurate estimates of the stellar masses with a minimum of model assumptions. If such systems have not yet experienced interaction, these are most easily linked to the initial masses of the components.

The most massive binary systems in the Galaxy with dynamically measured masses that are currently known are NGC3603-A1 (116 ± 31 and 89 ± 16 $M_\odot$; Schnurr et al. 2008), WR20a (83 ± 5 and 82 ± 5 $M_\odot$; Rauw et al. 2004; Bonanos et al. 2004). Other very massive binary systems include WR25 (Gamen et al. 2006) and WR21a. The latter, WR21a, is a possible addition to the list of most massive stars. WR21a is composed of a hydrogen-rich nitrogen se-

⋆ Based on observations collected under program IDs 085.D-0704, 086.D-0446, 089.C-0874 and 090.D-0212 at the European Organisation for Astronomical Research in the Southern Hemisphere, Chile.

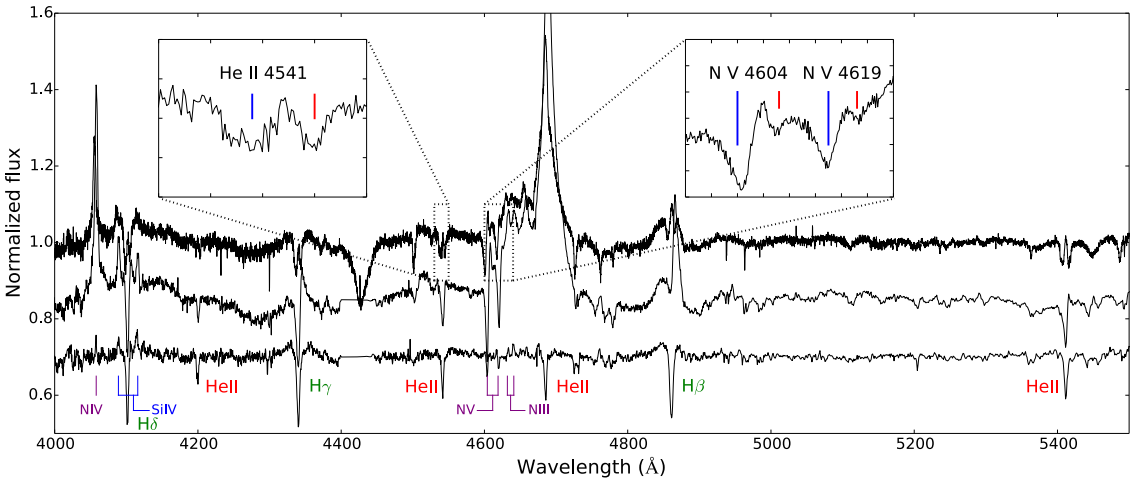

Figure 1. Rectified X-Shooter UVB spectrum of WR21a at epoch 16 (top spectrum), and the disentangled spectra of the primary and secondary components (middle and bottom spectra, respectively, and both displaced from unity for clarity). The insets show two of the SB2 lines used for the RV measurements, in which the redshifted contribution of the primary is indicated by the blue line and the blueshifted contribution of the secondary in red.

quence Wolf-Rayet (WNha) star and an early-type O star (Niemela et al. 2008, henceforth N08).

The WNh component of WR21a is the first Wolf-Rayet star detected through its bright X-ray emission (Caraveo et al. 1989; Mereghetti et al. 1994). WR21a also has weak non-thermal radio emission (Benaglia et al. 2005). Both the X-ray and radio emission are indicative of a colliding-wind region. Its projected location close to Westerlund 2 suggests that WR21a might have been ejected from this cluster.

N08 performed the first multi-epoch spectroscopic study of WR21a, and found an orbital period $P = 31.673 \pm 0.002$ d and an eccentricity $e = 0.64 \pm 0.03$. They infer minimum masses of 87 $M_\odot$ for the WN star and 53 $M_\odot$ for the O star, placing the system amongst the highest-mass Galactic binaries known. However, the orbital solution of N08 for the secondary component is based on a limited number of measurements of He IIλ5412. New high-quality data are required to better constrain the orbital and physical properties of this corner-stone system.

As part of the NOVA program for VLT/X-Shooter guaranteed time, we obtained multi-epoch, intermediate- to high-resolution spectra of WR21a. Our spectra reveal multiple SB2 lines, which allow for a firm determination of the orbit of both components and of their minimum masses and spectral types. In this paper, we use these constraints to estimate the absolute masses of the WR21a components. A quantitative spectroscopic analysis will be the focus of a later work.

This paper is organized as follows. The next Section gives an overview of the observations and data reduction. Section 3 presents the radial-velocity measurements and derives the new orbital solution. Section 4 discusses absolute mass estimates and the systems origin and evolutionary state. We summarize our findings in Section 5.

2 OBSERVATIONS AND DATA REDUCTION

All observations of WR21a have been obtained with the X-Shooter spectrograph (Vernet et al. 2011) mounted on the European Southern Observatory's *Very Large Telescope*. The observational campaign has been designed to intensively cover the January 2011 periastron passage, as well as to provide coverage of the orbit on longer timescales. The journal of the observations including radial-velocity measurements (see Section 3) can be found in Appendix A.

The data have been obtained in nodding mode, with a minimum of two exposures per data set. Each individual observation had an exposure time of 90 s, and was obtained with a 0.5″ slit for the UVB arm (3000 to 5500 Å) and 0.4″ slits for the VIS (5500 to 10 000Å) and NIR arms (10 000 to 25 000 Å). These slit widths result in a spectral resolving power $R = \lambda/\Delta\lambda$ of 9900, 18 200, and 10 500 in the three arms, respectively. Only the data from the UVB arm are used in the present paper.

The data have been reduced using the X-Shooter pipeline v2.4.0 under the automated REFLEX environment. The resulting 1D flux-calibrated spectra were normalized by fitting a sixth degree polynomial to the continuum and dividing the flux by the resulting function. Finally, the data were corrected for the barycentric motion at the time of observations. The last four epochs in our time series (#23-26) present low-frequency continuum fluctuations that may be related to poor performances of the atmospheric dispersion corrector (ADC) and/or poorly defined blaze functions. A local renormalization was applied to compensate for these effects so that they do not impact our radial-velocity (RV) measurements.

3 ORBITAL PROPERTIES

3.1 Radial Velocities

The X-Shooter UVB spectra of WR21a present a mix of absorption and emission lines of predominantly H, He and N (see Fig. 1). All the lines are variable in position and some of them also in shape. The strongest emission lines are those of He IIλ4686 and N IVλ4058 (see Fig. 2), which are single-lined and trace the orbital motion of the WR component. Hβ

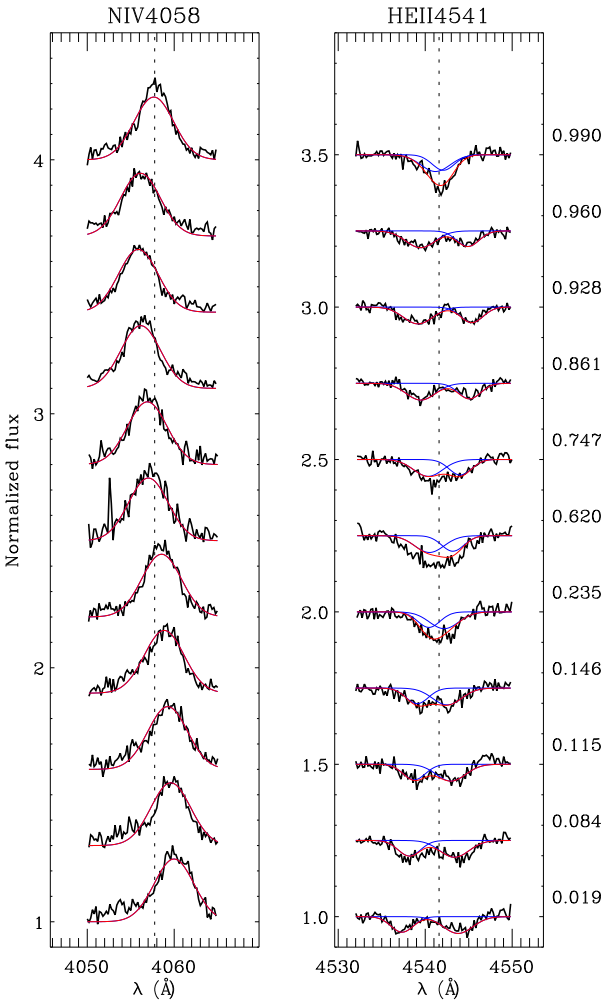

Figure 2. Variations of the N IVł4058 and He IIł4541 lines as a function of the phase (right-hand side scale). The best-fit Gaussian profiles used for RV determination have been overlaid.

presents a strongly variable profile with mixed absorption and emission. Hγ, Hδ and N V $\lambda\lambda$4604-4619 are double-lined and dominated by absorption but exhibit a small emission component on their red wing. This indicates that one of the two components may have a weak P-Cygni profile. Finally, the He II $\lambda\lambda$4200, 4541 and 5412 lines show a clear double-lined profile with both components in absorption and with intensities of the order of 5% or less of the continuum level. No trace of He I is seen in the WR21a spectrum, suggesting both stars to be hot enough to fully ionize helium. High temperatures are also supported by the presence of N V lines in both stars.

To measure the radial velocities (RVs) of the two components, we focus on the He II and H8 absorption lines and on the N IVł4058 emission. We first fitted each spectral line separately using one or two Gaussian functions for single- and double-lined profiles, respectively. We follow the approach described in Sana et al. (013a) and successfully applied to X-Shooter data in Sana et al. (013b). For each spectral line, we fitted one Gaussian profile for each of the two components and we used the same Gaussian profiles to fit all epochs simultaneously. With the exception of two spectra taken at orbital phase $\phi \approx 0.6 - 0.7$ and discussed further below, no strong line profile variations are seen for the considered lines, so that the assumption of keeping the shape of the line profiles fixed is valid. The adopted approach greatly improved the robustness of the RV measurements for our lower signal-to-noise ratio data and for epochs where the lines of the two components are blended.

The RVs measured from the individual lines appear to be compatible with each other, but for a possible systematic shift. Such a shift may be the result of the lines forming in different zones of the outflowing atmospheres. We thus decided to fit all the lines simultaneously. We required that, for a given epoch and a given stellar component, all the lines yield the same RV shift. As additional free parameters, we added a systematic zero point shift ($\delta\gamma$) of the RV measured from each line compared to the systemic velocity (γ) of the He IIł4541 line (see, e.g., Taylor et al. 2011). This brings all the measured velocities back onto the He IIł4541 RV reference frame.

3.2 Orbital solution

We computed an orbital solution using the RVs obtained by fitting the H8, N IVł4058 and He II $\lambda\lambda$4200, 4541, 5412 lines simultaneously. In this solution, three epochs provide larger residuals. These are at $\phi = 0.3$ (epoch #7), where the lines are strongly blended, and at $\phi = 0.72$ and 0.75 (epochs #24 and 25). For the latter two epochs, He IIł4541 is stronger than at other phases while H8 seems slightly weaker. The effect is however not as strong as for epoch #23 at $\phi = 0.62$ (Fig. 2). The change of line intensity seems most significant for the primary component. The N IVł4058 primary line and the He IIł5412 line, however, do not show correlated variations. Our final orbital solution excludes these epochs #7, 24 and 25 from the fit (see Figure 3). This results in slightly smaller residuals and error bars, but does not change significantly the fitted parameters (see Table 1).

Although over 50 epochs of observations are available from N08, we chose not to use these for our orbital solution. The selection of spectral lines that we use for our RV measurements are not available in N08 due to the lower signal-to-noise ratio, spectral resolution, and/or wavelength coverage of their data. Instead, N08 had to rely on somewhat challenging lines for their RV measurements (e.g., lines possibly affected by wind-wind collision contamination, by P-Cygni profiles, and/or by severe blending either between the contributions from the primary and the secondary or with nearby interstellar bands). Hence we feared that combining the N08 data set with ours may introduce systemetic biases, so that the resulting solution would not be more reliable than our standalone, homogeneously derived solution.

We find an orbital period of $P = 31.672 \pm 0.011$ d and a highly eccentric orbit ($e = 0.695 \pm 0.005$), which is similar to the values found by N08 ($P = 31.673 \pm 0.002$ d and $e = 0.64 \pm 0.03$). As our data show multiple SB2 lines at all epochs and our epochs cover the periastron passage, the orbit of both components is well constrained.

The minimum masses that we find are $M_1 \sin^3 i = 64.4 \pm 4.8$ M$_\odot$ and $M_2 \sin^3 i = 36.3 \pm 1.7$ M$_\odot$. These are considerably lower than the estimated 87 M$_\odot$ and 53 M$_\odot$ of N08. This results from the slightly larger eccentricity of

Table 1. Best-fit orbital solutions

		All data		Cleaned	
Parameter	Units	WR	O	WR	O
P	[d]	31.680 ± 0.013		31.672 ± 0.011	
e		0.694 ± 0.005		0.6949 ± 0.0047	
q	M_1/M_2	1.782 ± 0.030		1.776 ± 0.025	
T	$-2\,450\,000$	6345.43 ± 0.32		6345.20 ± 0.28	
ω	[°]	287.8 ± 1.2		287.2 ± 1.1	
K	[km s^{-1}]	157.0 ± 2.3	279.8 ± 6.2	156.9 ± 2.0	278.6 ± 5.3
γ	[km s^{-1}]	-32.8 ± 1.7	32.8 ± 2.9	-32.5 ± 1.6	32.0 ± 2.7
$M \sin^3 i$	[M$_\odot$]	65.3 ± 5.6	36.6 ± 1.9	64.4 ± 4.8	36.3 ± 1.7
rms	[km s^{-1}]	8.44		6.98	
$\delta\gamma(HeII\lambda4200)$	[km s^{-1}]	5.1 ± 4.0		4.8 ± 4.1	
$\delta\gamma(HeII\lambda5412$	[km s^{-1}]	-6.0 ± 2.6		-5.7 ± 2.7	
$\delta\gamma(H8)$	[km s^{-1}]	-5.2 ± 2.5		-5.9 ± 2.6	
$\delta\gamma(NIV\lambda4058)$	[km s^{-1}]	19.2 ± 2.4		19.8 ± 2.5	

our orbit compared to that of N08, and a difference in the derived semi-amplitudes of the RV curves.

4 DISCUSSION

In this Section we first derive the spectral types of both components, which give a crude estimate of their masses. We refine these estimates by using the total luminosity of the system as a mass indicator. Finally we discuss the potential origin of WR21a from Westerlund 2 and its evolutionary state.

4.1 Spectral types

To determine the spectral types of the components of WR21a, we first apply a new version of the disentangling code presented by Mahy et al. (2012) with, as third component, a spectral contribution from the interstellar medium. This code is based on the separation technique developed by Marchenko et al. (1998) and refined by González & Levato (2006), but uses Nelder & Mead's Downhill Simplex on the orbital parameters to reach the best χ^2 fit between the recombined component spectra and the observed data. In this process, we excluded the four spectra showing low frequency oscillation in the continuum (epochs #23 to 26), as described earlier. The disentangled spectra are shown in Fig. 1 and allow for an accurate spectral typing.

The primary late-type WN star shows hydrogen in its spectrum, and is thus of the WNh type. The presence of the N III $\lambda\lambda$4634-41 Å band and the absence of N IIIλ5314 Å indicates a spectral subtype of WN5, following the Smith et al. (1996) system. The primary spectrum shows absorption lines of He II and N V, and thus the 'a' suffix needs to be added (Smith et al. 1996). The presence of strong N V absorption indicates that this might be a transition star ('slash' star). We thus derive a spectral type for the primary of O3/WN5ha.

The spectrum of the secondary shows no sign of He I, indicating a spectral type earlier than O4. This is supported by the presence of N V $\lambda\lambda$4604-4619 absorption lines. The presence of N III emission lines excludes the O2 and O2.5 subtypes (Walborn et al. 2002). The relative strengths of the N III, N IV, and N V lines firmly constrain the spectral subtype to O3. The secondary has a strong He IIλ4686 absorption line, which is deeper than both He IIλ4200 and He IIλ4541, implying a Vz luminosity class. However, He IIλ4686 is likely affected by the colliding wind region and the disentangled profile might not be representative for the stellar spectrum, thus the z tag needs to be taken with caution. Finally, the presence of N IVλ4058, Si IVλ4089 and λ4116, and weak emission of N IIIλ4634-41 leads us to assign the secondary the spectral type O3Vz ((f*)).

To provide a first estimation of the absolute masses of the components, we use the Martins et al. (2005) spectral type calibration to estimate the mass of the secondary. We do this because the secondary follows a more standard classification scheme than the O3/WN5ha primary star, and thus more reliable mass calibrations exist. The mass of the secondary allows us to estimate the orbital inclination and primary mass from the orbital solution (Table 1).

Given that we can safely exclude the O2 V and O4 V spectral sub-types for the O star (see above), we consider that a one sub-type uncertainty on the spectral type corresponds to a 3σ error bar on the mass. Following Martins et al. (2005), we thus assign a typical mass of 58.3 ± 3.7 M$_\odot$ to the O3V secondary with a 1σ error bar. We derive an inclination of $58.8 \pm 2.5°$ and, correspondingly, a primary mass of 103.6 ± 10.2 M$_\odot$.

4.2 Absolute mass estimates

To further investigate the absolute masses of the components, we use the total luminosity of the system as a probe for the total mass. To do this, various assumptions have to be made. First, the reddening and total-to-selective extinction in the region of WR21a is highly variable. Here, we use the V-band magnitude and reddening from N08 and Roman-Lopes et al. (2011). This translates in a reddening corrected apparent V-band magnitude of $m_V = 7.3$. Second, the distance to WR21a is uncertain. Assuming the star originates from Westerlund 2, the distance to this cluster can be used as a probe for the distance to WR21a. However, several distance determinations to Westerlund 2 have been published, with estimates ranging between approximately 2 and 8 kpc. To account for this uncertainty, we calculate the luminos-

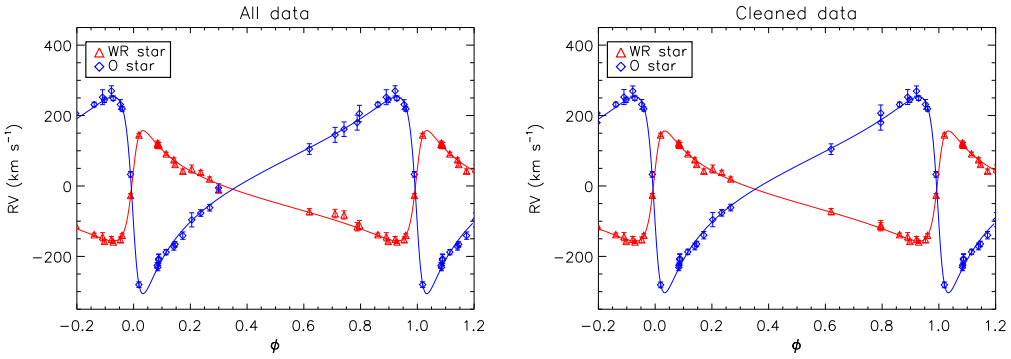

Figure 3. Best-fit orbital solutions obtained with all data (left) and with poor RV measurements removed (right).

Table 2. Adopted absolute V-band and bolometric magnitudes and their corresponding luminosities for three possible distances.

d (kpc)	M_V	$M_{\rm bol}$	$\log L/L_\odot$
2.85	−4.96	−8.96	5.48
6.0	−6.58	−10.58	6.13
8.0	−7.20	−11.20	6.38

ity for three recently published distances: 2.85 kpc (Carraro et al. 2013), 6 kpc (Hur et al. 2015), and 8 kpc (Rauw et al. 2007; Moffat et al. 1991). Third, a bolometric correction has to be assumed. As the luminosity is dominated by the WNh component, we assume a bolometric correction of 4.0, which is typical for WNh stars (Bestenlehner et al. 2014).

Table 2 lists the resulting absolute V and bolometric magnitudes and the corresponding luminosities for each of the above three distances. To translate the luminosities into masses, we use the Baysian interpolation method BONNSAI[1] (Schneider et al. 2014) to compare the luminosities with evolutionary tracks. This provides us with statistically meaningful error bars on the derived masses. This approach assumes that the stars have no prior history of interaction.

Although WR21a is a Galactic star, we use the evolutionary tracks for LMC metallicity (Brott et al. 2011; Köhler et al. 2015) to probe the mass-luminosity relation appropriate for the total system mass, as these are the only tracks currently available in BONNSAI that reach luminosities high enough for our purpose. We use a Salpeter initial mass function (Salpeter 1955) and the rotational velocity distribution from Ramírez-Agudelo et al. (2013) as priors. We derive the mass-luminosity relation for two ages of the system: the components being close to the zero-age main sequence (ZAMS, input age 0.1 ± 0.1 Myr) and the components having an age comparable to Westerlund 2 (input age 1.5 ± 0.5 Myr).

We derive luminosities for current primary masses of $70\,M_\odot \leqslant M_1 \leqslant 115\,M_\odot$ in steps of $5\,M_\odot$, and corresponding secondary masses following from the mass ratio of our orbital solution (Table 1). The relative error bars on the masses are set from the orbital solution as well. The resulting total-mass

[1] The BONNSAI web-service is available at www.astro.uni-bonn.de/stars/bonnsai.

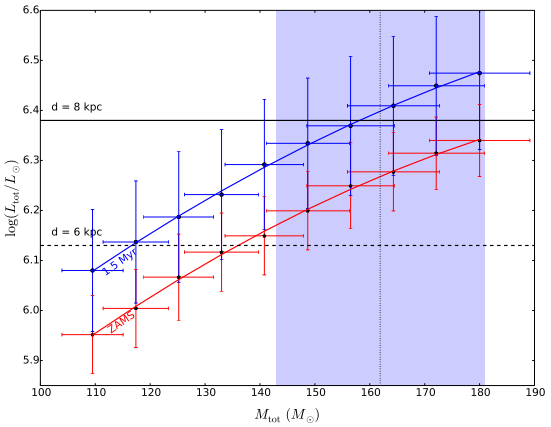

Figure 4. Total mass versus total luminosity relations derived from evolutionary tracks for ages close to the ZAMS (red) and 1.5 ± 0.5 Myr (blue). Also indicated are the observed total luminosities for distances of 6 kpc (dashed line) and 8 kpc (solid line). The total system mass that is estimated from the spectral type of the secondary is indicated with the shaded region, and is in agreement with a distance of 8 kpc and an age of 1.5 Myr.

versus total-luminosity relations are shown in Figure 4, and the grid of masses and luminosities is given in Table B1.

Figure 4 additionally shows the derived system luminosities for a distance of 6 and 8 kpc from Table 2. Our total mass estimate derived from the spectral type of the secondary is indicated as well. It can immediately be concluded that a distance of 2.85 kpc can be excluded for WR21a, as this corresponds to current masses that are a factor of two lower than the minimum masses obtained from our orbital solution.

Assuming that the distance to WR21a is indeed between 6 and 8 kpc, Figure 4 shows that the current system mass is approximately $130\,M_\odot \leqslant M_{\rm tot} \leqslant 200 M_\odot$ if the system is close to the ZAMS, and approximately $110\,M_\odot \leqslant M_{\rm tot} \leqslant 170 M_\odot$ for an age of 1.5 Myr. It is interesting to see that the total system mass of $M_{\rm tot} = 161.9 \pm 19.0\,M_\odot$ that is derived from the spectral type of the secondary is in excellent agreement with the system luminosity at a distance of 8kpc and an age of 1.5 Myr.

The uncertainty in our mass estimates imposed by the use of LMC evolutionary tracks is dominated by the amount

of mass that is lost during the evolution. To quantify this difference in mass, we estimate the mass loss at LMC metallicity and scale this to the solar value. To do this, we use our mass estimate of the secondary star as *initial* mass (as we have meaningful error bars on this value). We then use BONNSAI to quantify the amount of mass that this star would lose in 1.5 Myr at LMC metallicity. This mass loss amounts to $\Delta M_{2,1.5\mathrm{Myr}} \approx 2.5\,M_\odot$. Given that the mass loss is proportional to $Z^{0.7}$ (e.g., Vink et al. 2001; Mokiem et al. 2007), the mass loss of the secondary amounts to $\Delta M_2 \approx 4.1\,M_\odot$ at solar metallicity. In this example, the total current system mass is $155.0 \pm 13.7\,M_\odot$ for LMC metallicity, and $150.4 \pm 13.7\,M_\odot$ for Galactic metallicity. Thus, the uncertainty in the total mass imposed through our use of LMC tracks is on the order of $5\,M_\odot$ for a secondary mass of around $50 - 60\,M_\odot$, and lower for a lower mass. The derived total masses for LMC and Galactic metallicity remain well within error bars of each other.

Finally, we compare a total system luminosity of $\log(L/L_\odot) = 6.38$ ($\log(L_1/L_\odot) \approx 6.25$ and $\log(L_2/L_\odot) \approx 5.8$) to the tracks for Galactic metallicity from Ekström et al. (2012), which go up to $120\,M_\odot$. While this comparison is much less accurate than the BONNSAI method, these luminosities correspond to masses of approximately $M_1 \approx 100\,M_\odot$ and $M_2 \approx 60\,M_\odot$ at the ZAMS. This is in excellent agreement with our results from the LMC tracks.

4.3 Origin and evolutionary state

Due to its projected distance of $16'$ from the massive Westerlund 2 cluster, it has been suggested that WR21a originates from this cluster. Roman-Lopes et al. (2011) proposed that WR21a might have been dynamically ejected from the Westerlund 2 core, together with the massive binaries WR20aa and WR20c. These stars are in a similar geometrical configuration in the plane of the sky as AE Aur, μ Col, and ι Ori, for which a binary ejection scenario has been proposed (Blaauw 1961). Disruption of the orbit by dynamical interactions may explain the high eccentricity of the WR21a system, which is higher than any other massive binary with similar period (Sana et al. 2012). The systematic radial velocity of WR21a that follows from our orbital solution is comparable to that of Westerlund 2 (Rauw et al. 2011), and thus there is no indication for a significant runaway motion in the line of sight if the system indeed originates from this cluster. At the maximum distance estimate of 8 kpc, the projected distance of WR21a from Westerlund 2 is 37 pc. WR21a would have to travel at a speed of 36 km s^{-1} along the plane of the sky in order to reach its current position within 1 Myr. This is well within the maximum velocity at which a massive binary can be ejected (Perets & Šubr 2012).

The derived spectral types of the components of WR21a can be used to estimate their evolutionary state. Hydrogen rich WN stars are very massive main sequence stars that are so luminous that their winds are optically thick (de Koter et al. 1997). They are located close to the ZAMS in the Hertzsprung-Russell diagram (HRD) (e.g., Hamann et al. 2006), and thus the primary O3/WN5ha star is expected to be very young, likely around 1–2 Myr. The O3 secondary star is expected to be of similar age, as stars this massive will evolve towards later spectral types within 2 Myr unless they are rotating rapidly (e.g. Brott et al. 2011). The full width at half maximum of He IIλ4541 Å (3.0206 ± 0.0996 Å) indicates a rotational velocity of $v_{\mathrm{rot}} \sin i \approx 66$ km s^{-1} following the Ramírez-Agudelo et al. (2015) calibration ($v_{\mathrm{rot}} = 77$ km s^{-1} for an inclination $i = 58.8^\circ$). Thus, we have no indication for such rapid rotation.

5 SUMMARY AND CONCLUSIONS

We have presented multi-epoch observations of the massive binary system WR21a, including a full coverage of the January 2011 periastron passage. The data allow us to obtain orbital solutions for both components of WR21a. We derive very accurate minimum masses of $M_1 \sin^3 i = 64.4 \pm 4.8$ M$_\odot$ and $M_2 \sin^3 i = 36.3 \pm 1.7$ M$_\odot$.

We derive spectral types O3/WN5ha and O3Vz ((f*)) for the primary and secondary, respectively. From the spectral type of the secondary we estimate an absolute mass of $M_2 = 58.3 \pm 3.7$ M$_\odot$. This indicates an inclination of $i = 58.8 \pm 2.5^\circ$ and a primary mass of $M_1 = 103.6 \pm 10.2$ M$_\odot$, making the primary the second most massive star with dynamically measured mass in the Galaxy.

The spectral appearance of WR21a is compatible with an age of 1.5 Myr, similar to that of Westerlund 2. A total system mass of $M_{\mathrm{tot}} = 161.9 \pm 19.0\,M_\odot$, derived from the spectral type of the secondary, and a total system luminosity of $\log(L_{\mathrm{tot}}/L_\odot) = 6.38$ for a distance of 8 kpc, is in good agreement with the mass-luminosity relation predicted by evolutionary models.

Spectral disentangling will allow us to quantitatively analyse the spectra of both components and obtain their stellar and wind parameters. Comparison of these parameters with evolutionary tracks gives a stronger constraint on the ages of the components, and will give more insight in the evolutionary state of the system. The study of the colliding wind region in X-rays may provide independent constraints on the orbital inclination, and allow us to confirm the absolute masses found in this study. These studies are planned for a future publication on this system. Finally, linear broadband polarimetry as well as a precision light curve may allow us to obtain independent estimates of the orbital inclination (St.-Louis et al. 1987; Lamontagne et al. 1996).

REFERENCES

Benaglia P., Romero G. E., Koribalski B., Pollock A. M. T., 2005, A&A, 440, 743

Bestenlehner J. M., Gräfener G., Vink J. S., Najarro F., de Koter A., Sana H., Evans C. J., Crowther P. A., Hénault-Brunet V., Herrero A., Langer N., Schneider F. R. N., Simón-Díaz S., Taylor W. D., Walborn N. R., 2014, A&A, 570, A38

Bestenlehner J. M., Vink J. S., Gräfener G., et al. 2011, A&A, 530, L14

Blaauw A., 1961, Bull. Astron. Inst. Netherlands, 15, 265

Bonanos A. Z., Stanek K. Z., Udalski A., et al. 2004, ApJ, 611, L33

Brott I., de Mink S. E., Cantiello M., et al. 2011, A&A, 530, A115

Caraveo P. A., Bignami G. F., Goldwurm A., 1989, ApJ, 338, 338

Carraro G., Turner D., Majaess D., Baume G., 2013, A&A, 555, A50
Crowther P. A., Schnurr O., Hirschi R., et al 2010, MNRAS, 408, 731
de Koter A., Heap S. R., Hubeny I., 1997, ApJ, 477, 792
Ekström S., Georgy C., Eggenberger P., Meynet G., Mowlavi N., Wyttenbach A., Granada A., Decressin T., Hirschi R., Frischknecht U., Charbonnel C., Maeder A., 2012, A&A, 537, A146
Figer D. F., 2005, Nature, 434, 192
Gamen R., Gosset E., Morrell N., Niemela V., Sana H., Nazé Y., Rauw G., Barbá R., Solivella G., 2006, A&A, 460, 777
González J. F., Levato H., 2006, A&A, 448, 283
Hamann W.-R., Gräfener G., Liermann A., 2006, A&A, 457, 1015
Hur H., Park B.-G., Sung H., Bessell M. S., Lim B., Chun M.-Y., Sohn S. T., 2015, MNRAS, 446, 3797
Köhler K., Langer N., de Koter A., de Mink S. E., Crowther P. A., Evans C. J., Gräfener G., Sana H., Sanyal D., Schneider F. R. N., Vink J. S., 2015, A&A, 573, A71
Lamontagne R., Moffat A. F. J., Drissen L., Robert C., Matthews J. M., 1996, AJ, 112, 2227
Mahy L., Gosset E., Sana H., et al. 2012, A&A, 540, A97
Marchenko S. V., Moffat A. F. J., Eenens P. R. J., 1998, PASP, 110, 1416
Martins F., Schaerer D., Hillier D. J., 2005, A&A, 436, 1049
Mereghetti S., Belloni T., Shara M., Drissen L., 1994, ApJ, 424, 943
Moffat A. F. J., Shara M. M., Potter M., 1991, AJ, 102, 642
Mokiem M. R., de Koter A., Vink J. S., Puls J., Evans C. J., Smartt S. J., Crowther P. A., Herrero A., Langer N., Lennon D. J., Najarro F., Villamariz M. R., 2007, A&A, 473, 603
Niemela V. S., Gamen R. C., Barbá R. H., et al. 2008, MNRAS, 389, 1447
Perets H. B., Šubr L., 2012, ApJ, 751, 133
Ramírez-Agudelo O. H., Sana H., de Mink S. E., Hénault-Brunet V., de Koter A., Langer N., Tramper F., Gräfener G., Evans C. J., Vink J. S., Dufton P. L., Taylor W. D., 2015, ArXiv e-prints
Ramírez-Agudelo O. H., Simón-Díaz S., Sana H., de Koter A., Sabín-Sanjulían C., de Mink S. E., Dufton P. L., Gräfener G., Evans C. J., Herrero A., Langer L., 2013, A&A, 560, A29
Rauw G., De Becker M., Nazé Y., et al 2004, A&A, 420, L9
Rauw G., Manfroid J., Gosset E., Nazé Y., Sana H., De Becker M., Foellmi C., Moffat A. F. J., 2007, A&A, 463, 981
Rauw G., Sana H., Nazé Y., 2011, A&A, 535, A40
Roman-Lopes A., Barba R. H., Morrell N. I., 2011, MNRAS, 416, 501
Salpeter E. E., 1955, ApJ, 121, 161
Sana H., de Koter A., de Mink S. E. e. a., 2013a, A&A, 550, A107
Sana H., de Mink S. E., de Koter A., et al. 2012, Science, 337, 444
Sana H., Le Bouquin J.-B., Lacour S., et al. 2014, ApJS, 215, 15
Sana H., van Boeckel T., Tramper F., et al. 2013b, MNRAS, 432, L26
Schneider F. R. N., Izzard R. G., de Mink S. E., et al. 2014, ApJ, 780, 117
Schnurr O., Casoli J., Chené A.-N., Moffat A. F. J., St-Louis N., 2008, MNRAS, 389, L38
Smith L. F., Shara M. M., Moffat A. F. J., 1996, MNRAS, 281, 163
St.-Louis N., Drissen L., Moffat A. F. J., Bastien P., Tapia S., 1987, ApJ, 322, 870
Taylor W. D., Evans C. J., Sana H., Walborn N. R., de Mink S. E., Stroud V. E., Alvarez-Candal A., Barbá R. H., Bestenlehner J. M., Bonanos e. a., 2011, A&A, 530, L10
Vernet J., Dekker H., D'Odorico S., Kaper L., Kjaergaard P., Hammer F., Randich S., Zerbi F., et al. 2011, A&A, 536, A105
Vink J. S., de Koter A., Lamers H. J. G. L. M., 2001, A&A, 369, 574
Walborn N. R., Howarth I. D., Lennon D. J., et al. 2002, AJ, 123, 2754

APPENDIX A: JOURNAL OF OBSERVATIONS AND RADIAL VELOCITY MEASUREMENTS

Table A1 presents the journal of observations. Given are the Heliocentric Julian Date (HJD), exposure time ($t_{\rm exp}$), average airmass and spectral signal-to-noise (S/N) of each epoch. Additionally, the derived phase (ϕ) and the radial velocity measurements (RV) of both components of WR21a are listed.

APPENDIX B: GRID OF BONNSAI RUNS

The BONNSAI runs used to derive the total-mass versus total-luminosity relations are listed in Table B1. Columns 1–2 give the input masses, column three the corresponding total system mass, columns 4–5 the derived luminosities for both components for an age close to the ZAMS (0.1 ± 0.1 Myr), column 6 the corresponding system luminosity, columns 7–8 the derived luminosities for both components for an age of 1.5 ± 0.5 Myr, and column 9 the corresponding system luminosity.

Table A1. Journal of the observations.

Epoch	HJD[a] −2450000	$t_{\rm exp}$ (s)	Average airmass	S/N[b]	ϕ	$\rm RV_{WR}$ ($\rm km\,s^{-1}$)	$\rm RV_{O}$ ($\rm km\,s^{-1}$)
1	5302.6722	4×90	1.36	56	0.083	122.2 ± 5.5	-231.1 ± 9.6
2	5304.4679	4×90	1.32	52	0.140	74.2 ± 5.8	-171.7 ± 9.7
3	5305.4683	4×90	1.31	46	0.171	42.1 ± 6.3	-139.8 ± 10.5
4	5306.4652	4×90	1.31	23	0.203	48.2 ± 11.4	-95.7 ± 20.1
5	5307.4700	4×90	1.29	52	0.235	38.5 ± 5.8	-76.2 ± 9.4
6	5308.4729	4×90	1.28	54	0.266	19.8 ± 5.9	-61.2 ± 9.6
7[c]	5309.4631	4×90	1.30	40	0.298	-11.4 ± 4.9	-5.3 ± 8.1
8	5334.4549	4×90	1.20	34	0.087	115.1 ± 8.1	-209.5 ± 15.1
9	5334.4626	4×90	1.20	38	0.087	116.6 ± 7.4	-206.0 ± 13.6
10	5451.9898	2×90	2.64	20	0.795	-110.8 ± 13.1	206.8 ± 23.3
11	5454.9112	4×90	2.45	22	0.890	-144.1 ± 11.8	252.6 ± 21.3
12	5455.8989	4×90	2.63	33	0.921	-151.6 ± 8.2	269.5 ± 14.6
13	5456.8984	4×90	2.59	34	0.953	-152.8 ± 8.0	231.7 ± 13.8
14	5580.6941	8×90	1.37	76	0.861	-138.4 ± 4.6	231.4 ± 6.7
15	5581.8381	8×90	1.22	68	0.898	-157.5 ± 4.9	244.6 ± 7.4
16	5582.8155	8×90	1.20	78	0.928	-159.0 ± 4.5	249.5 ± 6.6
17	5583.8132	8×90	1.20	78	0.960	-140.0 ± 4.5	219.3 ± 6.6
18	5584.7597	8×90	1.21	69	0.990	-26.7 ± 5.2	32.9 ± 8.0
19	5585.6929	8×90	1.33	67	0.019	145.0 ± 4.9	-280.9 ± 8.1
20	5587.7343	8×90	1.23	64	0.084	117.3 ± 5.1	-224.9 ± 8.5
21	5588.7303	8×90	1.23	70	0.115	91.2 ± 4.8	-187.2 ± 7.6
22	5589.7163	8×90	1.25	68	0.146	61.2 ± 4.9	-164.7 ± 7.7
23	5604.7212	6×90	1.20	31	0.620	-72.7 ± 8.8	104.5 ± 15.1
24[c]	6114.4800	6×90	1.51	22	0.715	-78.4 ± 8.5	145.2 ± 15.0
25[c]	6115.4785	6×90	1.51	23	0.747	-82.3 ± 8.3	161.2 ± 14.6
26	6338.7075	6×90	1.20	22	0.795	-115.6 ± 12.1	179.9 ± 21.3

Notes:
(a) Heliocentric Julian Date at mid-exposure;
(b) Signal-to-noise ratio per 0.2 Å bin in the $4250-4300$Å region;
(c) Not used in the final solution.

Table B1. Grid of BONNSAI runs.

			ZAMS			1.5 ±0.5 Myr		
M_1 ($M_\odot$)	M_2 ($M_\odot$)	$M_{\rm tot}$ ($M_\odot$)	$\log(L_1/L_\odot)$	$\log(L_2/L_\odot)$	$\log(L_{\rm tot}/L_\odot)$	$\log(L_1/L_\odot)$	$\log(L_2/L_\odot)$	$\log(L_{\rm tot}/L_\odot)$
70.0 ± 5.3	39.5 ± 1.9	109.5 ± 5.6	5.83 ± 0.06	5.34 ± 0.05	5.95 ± 0.08	5.97 ± 0.10	5.43 ± 0.07	6.08 ± 0.12
75.0 ± 5.6	42.4 ± 2.0	117.4 ± 6.0	5.88 ± 0.06	5.40 ± 0.05	6.00 ± 0.08	6.02 ± 0.10	5.51 ± 0.07	6.14 ± 0.12
80.0 ± 6.0	45.2 ± 2.1	125.2 ± 6.4	5.94 ± 0.07	5.47 ± 0.05	6.07 ± 0.09	6.07 ± 0.11	5.56 ± 0.07	6.19 ± 0.13
85.0 ± 6.4	48.0 ± 2.3	133.0 ± 6.8	5.99 ± 0.06	5.52 ± 0.05	6.12 ± 0.08	6.11 ± 0.11	5.62 ± 0.07	6.23 ± 0.13
90.0 ± 6.8	50.8 ± 2.4	140.8 ± 7.2	6.02 ± 0.06	5.56 ± 0.05	6.15 ± 0.08	6.17 ± 0.11	5.68 ± 0.07	6.29 ± 0.13
95.0 ± 7.1	53.7 ± 2.5	148.7 ± 7.6	6.07 ± 0.06	5.61 ± 0.05	6.20 ± 0.08	6.21 ± 0.11	5.73 ± 0.07	6.33 ± 0.13
100.0 ± 7.5	56.5 ± 2.7	156.5 ± 8.0	6.12 ± 0.07	5.66 ± 0.05	6.25 ± 0.09	6.24 ± 0.12	5.78 ± 0.07	6.37 ± 0.14
105.0 ± 7.9	59.3 ± 2.8	164.3 ± 8.4	6.14 ± 0.06	5.71 ± 0.05	6.28 ± 0.08	6.28 ± 0.12	5.82 ± 0.07	6.41 ± 0.14
110.0 ± 8.3	62.1 ± 2.9	172.1 ± 8.8	6.18 ± 0.06	5.74 ± 0.04	6.31 ± 0.07	6.32 ± 0.12	5.86 ± 0.07	6.45 ± 0.14
115.0 ± 8.6	65.0 ± 3.1	180.0 ± 9.2	6.20 ± 0.06	5.78 ± 0.04	6.34 ± 0.07	6.34 ± 0.13	5.90 ± 0.08	6.47 ± 0.15